Research Square

Preprints are preliminary reports that have not undergone peer review.
They should not be considered conclusive, used to inform clinical practice,
or referenced by the media as validated information.

# A Heptafurcated Optical-Fiber Bundle for Simultaneous Distance, Tilt Magnitude and Tilt-Axis Sensing

**G. Zubia**
University of the Basque Country (UPV/EHU)
**J. Zubia**
joseba.zubia@ehu.eus
University of the Basque Country (UPV/EHU)
**G. Aldabaldetreku**
University of the Basque Country (UPV/EHU)
**J. Amorebieta**
University of the Basque Country (UPV/EHU)
**O. Arrizabalaga**
University of the Basque Country (UPV/EHU)
**G. Durana**
University of the Basque Country (UPV/EHU)

**Research Article**

**Keywords:** optical fiber displacement sensor, intensity-modulated sensor, fiber bundle, angular displacement, tilt sensing, distance sensing, heptafurcated bundle, non-contact metrology

**Posted Date:** September 8th, 2026

**DOI:** https://doi.org/10.21203/rs.3.rs-10641276/v1

**License:** This work is licensed under a Creative Commons Attribution 4.0 International License.
Read Full License

**Additional Declarations:** No competing interests reported.

# A Heptafurcated Optical-Fiber Bundle for Simultaneous Distance, Tilt Magnitude and Tilt-Axis Sensing

G. Zubia[1], J. Zubia[2,3*], G. Aldabaldetreku[2], J. Amorebieta[4], O. Arrizabalaga[3,4], G. Durana[2,3]

[1]Department of Graphical Expression and Project Engineering, University of the Basque Country (UPV/EHU), Bilbao, 48013, Spain.
[2*]Department of Communications Engineering, University of the Basque Country (UPV/EHU), Bilbao, 48013, Spain.
[3]EHU Quantum Centre, University of the Basque Country (UPV/EHU), Bilbao, 48013, Spain.
[4]Department of Applied Mathematics, University of the Basque Country (UPV/EHU), Bilbao, 48013, Spain.

*Corresponding author(s). E-mail(s): joseba.zubia@ehu.eus;

**Abstract**

Reflective intensity-modulated optical-fiber sensors are attractive for non-contact metrology because they are compact, passive and robust. Conventional fiber-bundle architectures, however, generally measure either axial distance or angular displacement and do not simultaneously recover the three parameters required to characterize the target's axial position and angular orientation. The present work proposes a novel heptafurcated optical-fiber linear and angular displacement sensor (OFLADS) that simultaneously estimates target distance $\boldsymbol{d}$, tilt magnitude $\boldsymbol{\alpha}$ and tilt-axis azimuth $\boldsymbol{\Phi}$ from only six reflected-power measurements. The sensing head combines four directional receiving arms with two concentric receiving rings, thereby encoding directional and radial information within a single passive bundle. A complete forward model is developed, accounting for individual fiber contributions, finite-core coupling, numerical-aperture attenuation and mechanical admissibility. A physically structured reconstruction procedure first estimates $\boldsymbol{\Phi}$ from opposite-arm logarithmic ratios, then obtains initial values of $\boldsymbol{d}$ and $\boldsymbol{\alpha}$ from a calibrated map, and finally refines $\boldsymbol{d}$, $\boldsymbol{\alpha}$ and $\boldsymbol{\Phi}$ jointly using the full six-power vector while eliminating the unknown common gain analytically.

Experimental validation was performed at five representative operating conditions. This sensor exhibited mean absolute reconstruction errors of 1.63% for $\boldsymbol{d}$, 2.06% for $\boldsymbol{\alpha}$ and **0.87°** for $\boldsymbol{\Phi}$, with maximum absolute errors of 5.44%, 4.65% and **1.74°**, respectively. The OFLADS demonstrated herein shows promise as a compact and potentially low-cost solution for simultaneous three-parameter non-contact monitoring in positioning, alignment, robotic metrology and other industrial applications that are not readily addressed by conventional fiber-bundle sensors.

**Keywords:** optical fiber displacement sensor, intensity-modulated sensor, fiber bundle, angular displacement, tilt sensing, distance sensing, heptafurcated bundle, non-contact metrology

# 1 Introduction

Accurate non-contact measurement of displacement and angular orientation is increasingly required in applications where the target cannot be instrumented directly, such as turbomachinery monitoring, structural health monitoring, precision alignment, robotics and industrial metrology. In these environments, the sensing head may be exposed to vibration, temperature variations, electromagnetic interference, restricted optical access and severe space limitations. These requirements are consistent with the broader transition towards resilient and highly instrumented industrial systems often discussed in the context of Industry 5.0[1;2].

Optical fiber displacement sensors (OFDSs) are attractive under these conditions because the optical probe can be compact and passive, while the source, photodetectors and signal-conditioning electronics can be placed remotely. Reflective intensity-modulated OFDSs are especially appealing because their operating principle is simple: light is emitted towards a target, the reflected field is collected by one or more receiving fibers, and the detected optical powers are related to the target position and orientation. General reviews of displacement measurement highlight the relevance of optical methods for non-contact metrology[3]. In the specific case of fiber-bundle probes, early works demonstrated high-resolution reflective sensors and established the geometrical foundations of the power-coupling mechanism[4;5]. Differential and multi-branch arrangements were later introduced to improve sensitivity, reduce common-mode fluctuations and extend the useful range[6;7]. Subsequent theoretical and experimental studies refined the analysis of bundle probes, including single-mode illumination, asymmetric receiving layouts, concave mirrors, coupler-based probes and real target surfaces[8–12]. These contributions show that the spatial arrangement of the transmitting and receiving fibers is one of the main design variables controlling sensitivity, linearity, working range and robustness.

The simultaneous recovery of distance and angular orientation remains more difficult than pure displacement measurement. A change in distance modifies the width, amplitude and overlap of the reflected spot, while a change in target tilt displaces the spot laterally on the bundle face. In addition, the tilt-axis azimuth

redistributes the reflected power among receiving fibers located at different angular positions. Fiber-optic tilt sensors based on interferometric structures, fiber Bragg gratings, eccentric-core fibers, liquid-marble Fabry–Perot cavities or bio-inspired multi-axis layouts have shown high sensitivity and wide angular measurement capabilities[13–22]. However, these solutions are not designed to reconstruct distance and tilt simultaneously from a single intensity-based reflective fiber bundle.

Several reflective or intensity-modulated angular displacement sensors have addressed part of this problem[23–35]. Multi-axis angle and displacement systems based on grating reflectors have also been proposed[36]. Within the literature reviewed here, conventional reflective bundle OFDSs primarily target axial distance, whereas angular and attitude sensors generally recover one or more angular coordinates using different sensing or interrogation structures. Although these works provide important background, the present objective is much more challenging: to estimate the distance $d$, the tilt magnitude $\alpha$ and the tilt-axis azimuth $\Phi$ using a compact passive bundle and reflected-power measurements.

Recent work by Zubia and co-workers has moved OFDS design towards systematic, model-driven bundle engineering. A design method for trifurcated OFDSs showed that the geometry and size of the bundle can be selected from a predictive model to satisfy prescribed requirements[37]. This design path was further consolidated by high-performance extended-range OFDSs and by analytical models for angular displacement sensing[38;39]. The progression from database-driven design to more complex multi-branch geometries is summarized in[40].

Building on this development, the present paper proposes a new and more challenging heptafurcated optical-fiber linear and angular displacement sensor (OFLADS), implemented as a bundle-based OFDS, for simultaneous estimation of $d$, $\alpha$ and $\Phi$. The OFLADS combines four directional arms, arranged along the $+x$, $-x$, $+y$ and $-y$ directions, with two concentric receiving rings. The cross arms encode the directional imbalance caused by the lateral displacement of the reflected spot, whereas the inner and outer rings encode the radial redistribution of the reflected power. This separation of roles is the central idea of the method: the tilt-axis direction is first estimated from opposite-arm power ratios, and the remaining coupled distance–tilt problem is then solved using a projected arm observable together with the inner/outer ring response.

The reconstruction strategy follows three stages. First, the tilt-axis azimuth $\Phi$ is estimated from the log-ratio vector of the two opposite-arm pairs. Second, after this direction has been estimated, the arm responses are projected along the tilt direction and combined with the ring log-ratio to obtain an initial estimate of the target distance $d$ and tilt magnitude $\alpha$ from a calibrated full-model map. Third, the initial triplet $(d_0, \alpha_0, \widehat{\Phi}_0)$ is jointly refined by a six-power nonlinear inversion. This sequence combines physical interpretability with full-model accuracy: the log-ratio variables explain how the bundle encodes direction, the calibrated map reveals the distance–tilt coupling, and the final nonlinear fit uses all measured powers while compensating for the unknown common gain. The novelty of the present work therefore lies in the joint design of the directional–radial bundle geometry, the complete forward model and the physically structured inverse reconstruction.

**Table 1** Positioning of the OFLADS relative to representative optical-fiber approaches. The comparison concerns the measurement objective and interrogation architecture; reported ranges and resolutions are not included because they depend strongly on the particular operating range and experimental definition.

| **Approach** | **Recovered quantities** | **Sensing and interrogation principle** | **Representative literature** |
|---|---|---|---|
| Reflective bundle OFDSs | Primarily axial distance $d$ | Passive fiber bundle and scalar reflected-power measurement | 4;5;8;9;37;38 |
| Reflective angular OFSs | One angular displacement or surface slope | Two-fiber or differential intensity heads | 23;27;29;32–34 |
| Multi-axis tilt or attitude sensors | One or two angular coordinates | Interferometric, FBG, cavity or multi-axis transduction structures | 13;14;17;18;22 |
| Grating-based multi-axis systems | Multiple angles and displacement | Grating reflector with multi-axis optical readout | 36 |
| Present OFLADS | $d$, $\alpha$ and $\Phi$ simultaneously | Single passive reflective bundle and six scalar power channels | This work |

The remainder of this paper is organized as follows. Section 2 summarizes the forward mathematical model and defines the six measured powers and the observables used for reconstruction. Section 3 describes the fabricated OFLADS, the experimental setup and the measurement protocol used to validate the proposed sensing approach. Section 4 analyzes the cross-arm and ring responses and establishes the physical basis for separating the tilt-axis azimuth from the coupled distance–tilt response. Section 5 applies the proposed three-stage reconstruction strategy to measured examples and evaluates the resulting estimation errors. To keep the main text focused on the physical interpretation and experimental results, the complete model derivation, calibration-map construction, gain elimination and nonlinear inversion procedure are provided in Appendix A.

## 2 Summary of the mathematical model

The complete mathematical model is given in Appendix A. This section summarizes the forward model and the reconstruction variables used in the main text. The optical field emitted by the central transmitting fiber is represented by a Gaussian beam. After specular reflection on a tilted mirror, the center of the reflected spot is displaced on the bundle face, as represented in Fig. 1. If the target is at distance $d$, tilted by magnitude $\alpha$, and the in-plane tilt-axis azimuth is $\Phi$, the lateral spot displacement

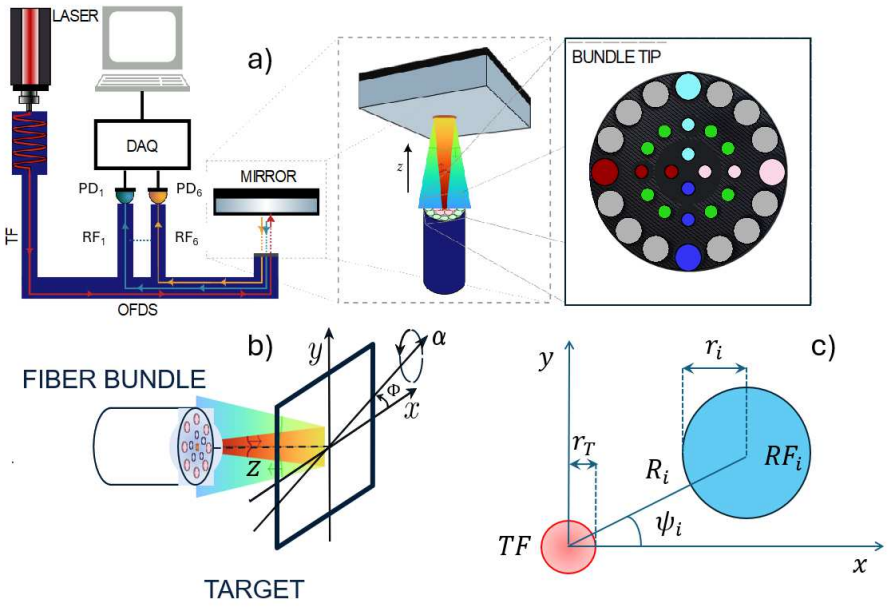



**Fig. 1** (a) Experimental setup of a typical OFLADS. It consists of a laser light-source, an optical fiber bundle to guide the light and several photodetectors (PDs), $\{\mathrm{PD}_1, \mathrm{PD}_2, \ldots, \mathrm{PD}_6\}$, which convert the optical power into electrical signals; these signals are digitized with a DAQ and transmitted to a computer for signal processing. (b) Definition of the target distance $d$, tilt magnitude $\alpha$ and tilt-axis azimuth $\Phi$. (c) Polar position $R_i$, azimuth $\psi_i$ and core radius $r_i$ of an arbitrary receiving fiber $\mathrm{RF}_i$, used in the forward model. TF denotes the transmitting fiber, and $r_T$ its core radius.

can be written as

$$\mathbf{s}(d, \alpha, \Phi) = S(d, \alpha)(\sin\Phi, -\cos\Phi), \qquad S(d, \alpha) = d\tan(2\alpha). \tag{2.1}$$

A receiving fiber centered at polar coordinates $(R_i, \psi_i)$ has squared distance to the spot center

$$\rho_i^2 = R_i^2 + S^2(d, \alpha) + 2R_i S(d, \alpha)\sin(\psi_i - \Phi). \tag{2.2}$$

This term contains the geometrical coupling between distance, tilt magnitude and tilt-axis azimuth. The approximate received power is[39]

$$P_i(d, \alpha, \Phi) = G\, g_{\mathrm{tot}}(d, \alpha; R_T) K_i(d, \alpha; r_i) \exp[-B(d, \alpha)\rho_i^2], \tag{2.3}$$

where $G$ is the single common optical–electronic scale factor. It includes the product of source power and target reflectivity, fiber losses, detector responsivity and electronic gain. The Gaussian decay coefficient $B$ and the geometrical finite-core factor $K_i$ are

$$B(d, \alpha) = \frac{2\cos^2(2\alpha)}{d^2[1 + \cos(2\alpha)]^2 \tan^2\theta_0}, \tag{2.4}$$

$$K_i(d,\alpha;r_i) = \frac{4r_i\cos^2(2\alpha)}{\pi d[1+\cos(2\alpha)]\tan\theta_0}\,\mathrm{erf}\left[\frac{2r_i\cos^2\alpha}{d[1+\cos(2\alpha)]\tan\theta_0}\right]. \tag{2.5}$$

The factor $g_{\mathrm{tot}}$ combines the numerical-aperture attenuation and the mechanical admissibility gate,

$$g_{\mathrm{tot}}(d,\alpha;R_T) = g_{\mathrm{NA}}(\alpha)g_{\mathrm{mech}}(d,\alpha;R_T). \tag{2.6}$$

The numerical-aperture factor accounts for the fact that the receiving fiber only accepts light within its acceptance cone. With $\theta_{\mathrm{NA}} = \arcsin(\mathrm{NA})$, it is written as

$$g_{\mathrm{NA}}(\alpha) = \begin{cases} 1, & |\alpha| + \theta_0 \le \theta_{\mathrm{NA}}, \\ \exp\left[-\left(\dfrac{|\alpha| + \theta_0 - \theta_{\mathrm{NA}}}{\sigma_{\mathrm{NA}}}\right)^2\right], & |\alpha| + \theta_0 > \theta_{\mathrm{NA}}. \end{cases} \tag{2.7}$$

The value $\sigma_{\mathrm{NA}} = 5^\circ$ was used throughout the model calculations. The mechanical gate enforces the physical clearance between the mirror and the bundle tip. In other words, it prevents the bundle tip from touching the mirror when it tilts,

$$g_{\mathrm{mech}}(d,\alpha;R_T) = H\left[\arctan\left(\frac{d}{R_T}\right) - |\alpha|\right]. \tag{2.8}$$

Because $g_{\mathrm{NA}}$ and $g_{\mathrm{mech}}$ multiply all six channels equally, they cancel from the power ratios and do not provide directional information. They are retained in the forward model to delimit the valid operating domain. Any candidate for which $g_{\mathrm{mech}} = 0$ is rejected before a logarithm is evaluated.

Table 2 shows the definition and physical meaning of the variables appearing in Eqs. (2.2)–(2.8).

Figure 2 shows a representation of the heptafurcated bundle geometry. The four directional arms are located at azimuths $\psi_i = 0$, $\pi$, $\pi/2$ and $3\pi/2$. Each arm contains three fibers at radii $R_i = 0.25$, 0.70 and 1.26 mm, with core radii $r_i = 0.11$, 0.11 and 0.22 mm. The inner ring contains eight fibers and the outer one, twelve.

The heptafurcated bundle is modeled by summing Eq. (2.3) over the fibers belonging to each collection. The six measured powers are collected in the vector

$$\mathbf{P} = [P_{+x}, P_{-x}, P_{+y}, P_{-y}, P_{\mathrm{in}}, P_{\mathrm{out}}]^{\mathsf{T}}. \tag{2.9}$$

The cross arms provide directional information, whereas the rings provide radial information. Changing the sign of $\alpha$ reverses the sign of the spot displacement and swaps the response of opposite arms, while the ring powers are nearly even in $\alpha$ and weakly dependent on $\Phi$. The first reconstruction step uses the opposite-arm log-ratios

$$L_x = \ln\left(\frac{P_{+x}}{P_{-x}}\right), \qquad L_y = \ln\left(\frac{P_{+y}}{P_{-y}}\right), \tag{2.10}$$

**Table 2** Definition and physical meaning of the variables appearing in Eqs. (2.2)–(2.8).

| Symbol | Definition and physical meaning |
|---|---|
| $P_i$ | Optical power collected by receiving fiber $i$. |
| $d$ | Axial distance between the bundle face and the mirror reference point. |
| $\alpha$ | Magnitude of the mirror tilt. |
| $\Phi$ | In-plane azimuth of the tilt axis. |
| $R_i$ | Radial distance from the bundle center to the center of receiving fiber $i$. |
| $\psi_i$ | Azimuthal coordinate of the center of receiving fiber $i$. |
| $r_i$ | Core radius of receiving fiber $i$. |
| $S(d,\alpha)$ | Magnitude of the lateral displacement of the reflected-spot center, $S = d\tan(2\alpha)$. |
| $\rho_i$ | Distance between the center of receiving fiber $i$ and the reflected-spot center. |
| $G$ | Single global scale accounting for source power, target reflectivity, fiber losses, detector responsivity and electronic gain. |
| $B(d,\alpha)$ | Gaussian spatial-decay coefficient of the reflected irradiance distribution. |
| $K_i(d,\alpha;r_i)$ | Finite-core coupling factor for receiving fiber $i$. |
| $\theta_0$ | Emission half-angle of the transmitting fiber. |
| $g_{\mathrm{tot}}$ | Total multiplicative factor combining numerical-aperture attenuation and mechanical admissibility. |
| $g_{\mathrm{NA}}$ | Numerical-aperture attenuation factor. |
| NA | Numerical aperture of the receiving fibers. |
| $\theta_{\mathrm{NA}}$ | Acceptance half-angle of the receiving fibers, $\theta_{\mathrm{NA}} = \arcsin(\mathrm{NA})$. |
| $\sigma_{\mathrm{NA}}$ | Angular width controlling the smooth attenuation beyond the acceptance cone; $\sigma_{\mathrm{NA}} = 5^\circ$. |
| $g_{\mathrm{mech}}$ | Mechanical admissibility gate that suppresses configurations in which the mirror would intersect the bundle tip. |
| $R_T$ | Outer radius of the bundle tip or ferrule used in the clearance condition. |
| $H(\cdot)$ | Heaviside step function used to impose the mechanical gate. |

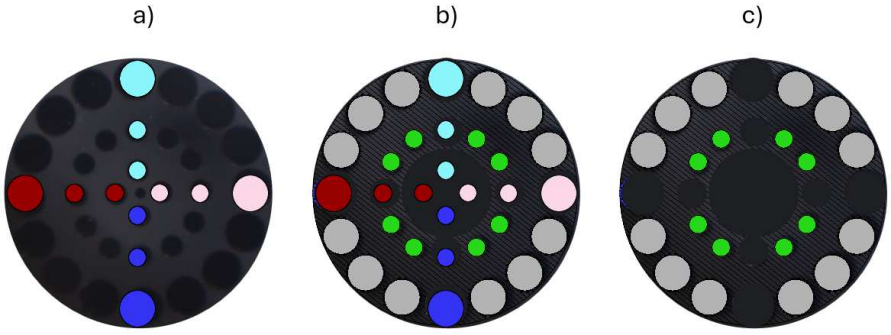



**Fig. 2** Bundle-tip views of the OFLADS sensor head. (a) Fabricated bundle end face, where the directional cross arms are visible. (b) Schematic of the complete fiber arrangement, including the four directional cross arms and the two concentric receiving rings. (c) Simplified representation of the concentric-ring subsystem. The cross-arm and ring responses provide the complementary directional and radial information used in the reconstruction.

**Table 3** Nominal geometry and numerical aperture of the OFLADS fibers. Radial distances are measured from the bundle center.

| Collection | Nominal geometry | NA | Channel |
|---|---|---|---|
| Illumination fiber | Central single-mode fiber; nominal core/cladding diameter 4/125 $\mu$m | $\approx 0.12$ | TF |
| $+x$ arm | Three receiving fibers at $R_i = 0.25$, 0.70, and 1.26 mm; core radii $r_i = 0.11$, 0.11, and 0.22 mm | 0.22 | $P_{+x}$ |
| $-x$ arm | Same radial positions as the $+x$ arm, opposite azimuth | 0.22 | $P_{-x}$ |
| $+y$ arm | Same radial positions as the $+x$ arm, azimuth $+90^\circ$ | 0.22 | $P_{+y}$ |
| $-y$ arm | Same radial positions as the $+x$ arm, azimuth $-90^\circ$ | 0.22 | $P_{-y}$ |
| Inner ring | Eight receiving fibers at $R_{\mathrm{in}} = 0.70$ mm; core radius $r_{\mathrm{in}} = 0.10$ mm | 0.22 | $P_{\mathrm{in}}$ |
| Outer ring | Twelve receiving fibers at $R_{\mathrm{out}} = 1.26$ mm; core radius $r_{\mathrm{out}} = 0.20$ mm | 0.22 | $P_{\mathrm{out}}$ |
| Mechanical radius | $R_T = 3$ mm for the bundle tip or ferrule | – | – |

or, equivalently, $L_x = 2\,\mathrm{atanh}(D_x)$ and $L_y = 2\,\mathrm{atanh}(D_y)$, where $D_x$ and $D_y$ are the corresponding normalized differential ratios. The tilt-axis azimuth is estimated as

$$\widehat{\Phi}_0 = \mathrm{atan2}(L_x, -L_y). \tag{2.11}$$

After $\widehat{\Phi}_0$ has been obtained, the arm response is projected along the estimated tilt direction and combined with the ring ratio,

$$L_{\parallel} = L_x \sin\widehat{\Phi}_0 - L_y \cos\widehat{\Phi}_0, \qquad Q = \ln\left(\frac{P_{\mathrm{out}}}{P_{\mathrm{in}}}\right). \tag{2.12}$$

The pair $(L_{\parallel}, Q)$ is used to obtain a calibrated-map initial estimate $(d_0, \alpha_0)$, and the triplet $(d_0, \alpha_0, \widehat{\Phi}_0)$ is jointly refined by a six-power nonlinear fit. The full inverse procedure is detailed in Appendix A.

# 3 Experimental validation

The purpose of the experiment is to validate a single compact fiber-bundle probe able to recover the target distance $d$, the tilt magnitude $\alpha$, and the tilt-axis azimuth $\Phi$ from intensity measurements. This section describes the manufactured OFLADS, the experimental set-up used to control the target position and orientation, and the measurement protocol used to obtain the six optical powers.

## 3.1 Experimental setup and protocol

The complete experimental set-up is shown in Fig. 3. The source was a 660 nm Fabry–Perot laser module (S4FC660, Thorlabs), coupled to the illumination single-mode fiber (nominal core/cladding diameter 4/125 $\mu$m and numerical aperture NA $\approx 0.12$). The sensor tip faced a flat mirror, which acted as the reflective target. The target position and orientation were controlled by a linear translation stage and an angular stage (Zaber). The six receiving fiber collections were connected to a set of PDA100A-EC

photodetectors (Thorlabs), one for each collection. The photodetector voltages were recorded with a DAQ6510 data-acquisition unit (Keithley).

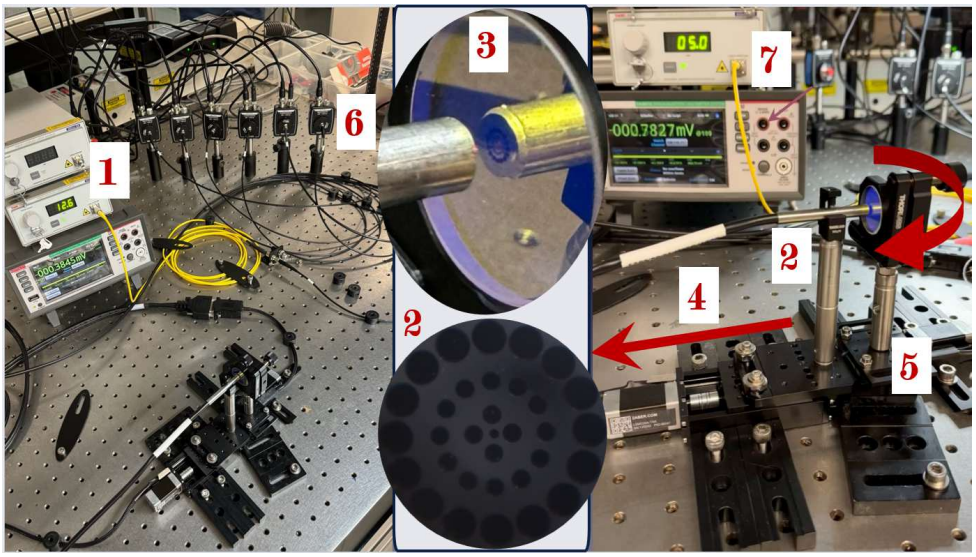



**Fig. 3** Experimental setup for validating the OFLADS. Left: Broad view of the setup, where (1) indicates the 660 nm laser source, (2) the OFLADS, (3) the mirror, (4) the linear stage, (5) the angular stage, (6) the set of PDs—one per RF collection—and (7) the acquisition unit. Top center: Close-up of the mirror (3) facing the OFLADS (2). Bottom center: Cross-section of the OFLADS. Right: Detailed view of the linear (4) and angular (5) stages, the mirror (3) and the OFLADS (2).

The stage assembly was arranged so that the axial translation controlled the distance $d$ between the mirror and the bundle face, while the angular stage controlled the tilt of the mirror. The zero-distance and zero-tilt references were established by aligning the mirror normal with the bundle axis and by centering the reflected signal with respect to the symmetric receiving collections. All channels were recorded simultaneously at each programmed stage position. At every programmed $(d, \alpha, \Phi)$ condition, three repeated acquisitions were obtained. Each experimental point, and therefore each experimental curve reported in this work, is the pointwise arithmetic mean of these three measurements. Before computing the reconstruction variables, the dark offsets of the photodetectors were subtracted. Channel-gain calibration factors can be applied at this stage when necessary.

Figure 4 illustrates a representative distance sweep used to equalize the four directional channels before reconstruction. The main plot shows the uncorrected responses of the four arms, for which different channel gains produce distinct amplitudes even when the qualitative trend is the same. The inset shows the corrected responses after gain equalization, where the four curves collapse to an almost common trajectory. This calibration step removes systematic differences among the receiving channels and allows the later use of ratios and logarithmic observables with significantly lower bias.

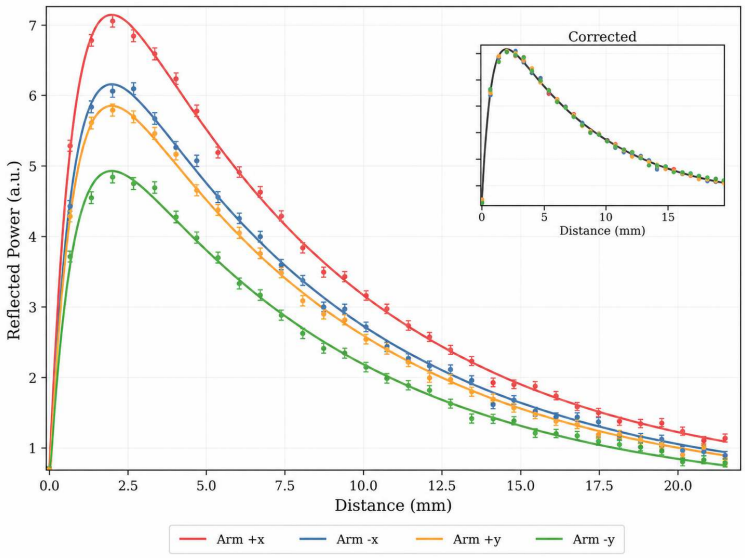



**Fig. 4** Representative distance response of the four receiving arms before calibration (main plot) and after channel-gain correction (inset). After calibration, the four arm responses practically coincide over the whole distance range.

## 3.2 Experimental observables and validation strategy

The four directional arms validate the tilt-sensitive part of the sensor. For one-axis angular tests, the response of one opposite-arm pair is dominant, while the orthogonal pair remains approximately symmetric. For general tilt-axis orientations, both pairs contribute. Logarithmic ratios are essential because they convert opposite-arm imbalance into an approximately linear angular observable and cancel common multiplicative factors. At short distances, the response of the individual fibers inside an arm can be partially resolved, and shoulders or asymmetric humps may appear in the total arm power. At intermediate distances, the response is smoother and more suitable for reconstruction.

The two concentric receiving rings validate the distance-sensitive part of the sensor. Instead of relying on a single absolute power, the ratio between the outer and inner ring powers is used because it suppresses common fluctuations in laser power, target reflectivity, and detector gain. The ring log-ratio $Q$ is nearly independent of the tilt-axis azimuth and is therefore well suited to separate the distance contribution from the directional information provided by the arms.

Photodetector noise propagates strongly through logarithmic ratios when one of the powers is small. After dark-offset subtraction, a measurement state was accepted only when every channel satisfied $P_i > 5\sigma_{\mathrm{dark},i}$, where $\sigma_{\mathrm{dark},i}$ is the standard deviation of the dark signal of channel $i$. States failing this criterion were rejected before calculating $L_x$, $L_y$ or $Q$. The quantity $L_{\mathrm{mag}} = \sqrt{L_x^2 + L_y^2}$ remains a warning indicator: when it approaches zero, the tilt-axis azimuth is physically ill-defined.

# 4 Results and discussion

This section summarizes the main response properties of the OFLADS and their consequences for simultaneous estimation of $d$, $\alpha$ and $\Phi$. Here the emphasis is on the physical interpretation of the responses and on the observables that are most useful for the inverse problem.

## 4.1 Cross-arm response as a function of tilt angle

Each cross arm is a compound detector, because the measured arm power is the sum of three individual fiber contributions located at different positions. For an arm at azimuth $\psi_a$, the total power is

$$P_a(d,\alpha,\Phi) = G\sum_{i=1}^{3} g_{\mathrm{tot}}(d,\alpha;R_T)K_i(d,\alpha;r_i)\exp\left[-B(d,\alpha)\rho_i^2(R_i,\psi_a;d,\alpha,\Phi)\right]. \quad (4.1)$$

where $\rho_i^2$ is given by Eq. (2.2). Thus, $S(d,\alpha)$ controls the magnitude of the spot displacement, whereas $\sin(\psi_a-\Phi)$ controls how that displacement is projected onto a given arm. Consequently, the same tilt magnitude can produce very different arm powers depending on the tilt-axis azimuth $\Phi$.

The model predicts clear symmetry relations. As Eqs. (2.2) and (4.2) show, for $\Phi = 0°$, the $+x$ and $-x$ arms are almost symmetric because the displacement has zero projection on the $x$ pair, whereas the $+y$ and $-y$ arms form the direction-sensitive pair. For $\Phi = 90°$, the situation is rotated by 90°, so the sensitive pair becomes the $x$ arms. For $\Phi = 45°$, both opposite-arm pairs contribute simultaneously and their responses are more balanced. These symmetries are the origin of the direct estimator of $\Phi$ based on the log-ratio vector $(L_x, -L_y)$.

Figure 5 summarizes the arm-power responses as a function of tilt angle for ten representative distances between 1 mm and 10 mm, for the three canonical tilt-axis orientations $\Phi = 0°$, 45° and 90°. In each figure, the solid curves correspond to the ideal model and the dashed curves to measured ones. The expected symmetry is clearly visible. For $\Phi = 0°$, the $x$-arm pair remains almost symmetric while the $y$-arm pair carries the signed angular information. For $\Phi = 90°$, the situation is rotated, and for $\Phi = 45°$ both opposite-arm pairs contribute. As the distance increases, the arm peaks decrease and broaden, so the contrast between neighbouring distances becomes progressively smaller and the inverse problem becomes more sensitive to perturbations.

A useful geometrical approximation for the peak position of a single fiber is obtained by minimizing $\rho_i^2$ with respect to the spot displacement. Since the optimum occurs near $S(d,\alpha) = -R_i\sin(\psi_a-\Phi)$, the peak angle satisfies approximately

$$\alpha_{\mathrm{peak},i} \simeq \frac{1}{2}\arctan\left[-\frac{R_i}{d}\sin(\psi_a-\Phi)\right]. \quad (4.2)$$

For two fibers $i$ and $j$ belonging to the same arm, the small-angle form of Eq. (4.2) gives

$$|\Delta\alpha_{\mathrm{peak},ij}| \simeq \frac{|R_i - R_j|}{2d} \, |\sin(\psi_a - \Phi)| \, . \tag{4.3}$$

Therefore, a larger radial spacing between the fibers, a shorter target distance, and a stronger projection of the reflected-spot displacement onto the arm increase the angular separation of their individual power maxima. In Fig. 5, this effect appears indirectly through the displacement, broadening and asymmetry of the total arm responses, because each plotted arm power is the sum of the three individual fiber contributions.

For a fixed tilt-axis azimuth $\Phi$, the largest power contrast occurs for the opposite-arm pair perpendicular to the tilt axis, for which $|\sin(\psi_a - \Phi)| = 1$. The reflected spot moves towards one member of this pair and away from the other, reducing $\rho_i^2$ and increasing the exponential coupling term in the favoured arm while increasing $\rho_i^2$ and reducing the collected power in the opposite arm. Reversing the sign of $\alpha$ interchanges the favoured and unfavoured arms. By contrast, the pair parallel to the tilt axis satisfies $\sin(\psi_a - \Phi) = 0$ and remains approximately power-balanced. Accordingly, Fig. 5 shows the largest $+y/-y$ power difference for $\Phi = 0°$, the largest $+x/-x$ difference for $\Phi = 90°$, and a directional response shared by both arm pairs for $\Phi = 45°$.

## 4.2 Cross-arm response as a function of distance

For a fixed $\alpha$ and $\Phi$, the arm power as a function of distance is generally non-monotonic. It first rises as the reflected spot grows and overlaps more efficiently with the arm fibers, reaches a maximum, and then decreases as the spot spreads and the collected power is diluted. This rise–peak–decay behaviour means that a single arm cannot provide a unique distance estimate over the full range. The same power value may occur before and after the maximum, and near the maximum the derivative with respect to distance is small.

Figure 6 extends the distance-response analysis to the four arms and to the three canonical azimuths $\Phi = 0°$, $45°$ and $90°$. Each plot contains several tilt angles. The figure shows that the peak location and height vary strongly with $\alpha$, because the reflected spot displacement $S(d, \alpha) = d\tan(2\alpha)$ changes both the overlap position and the beam width at the bundle face. The role of $\Phi$ is to determine which arm is favoured by the lateral displacement. For $\Phi = 0°$ the largest directional asymmetry appears mainly in the $y$ pair, while for $\Phi = 90°$ it appears mainly in the $x$ pair. At $\Phi = 45°$ the response is distributed between both pairs.

The distance response confirms that the four-arm subsystem contains rich directional information, but also that no individual arm can provide a unique and robust distance estimate over the full working range. Robust recovery of $d$ and $\alpha$ therefore requires combining all channels.

## 4.3 Ring powers as a function of $d$, $\alpha$ and $\Phi$

The concentric receiving rings provide information that is fundamentally different from that supplied by the directional cross arms. Whereas the cross arms encode the orientation of the reflected spot over the bundle face, the ring responses are mainly

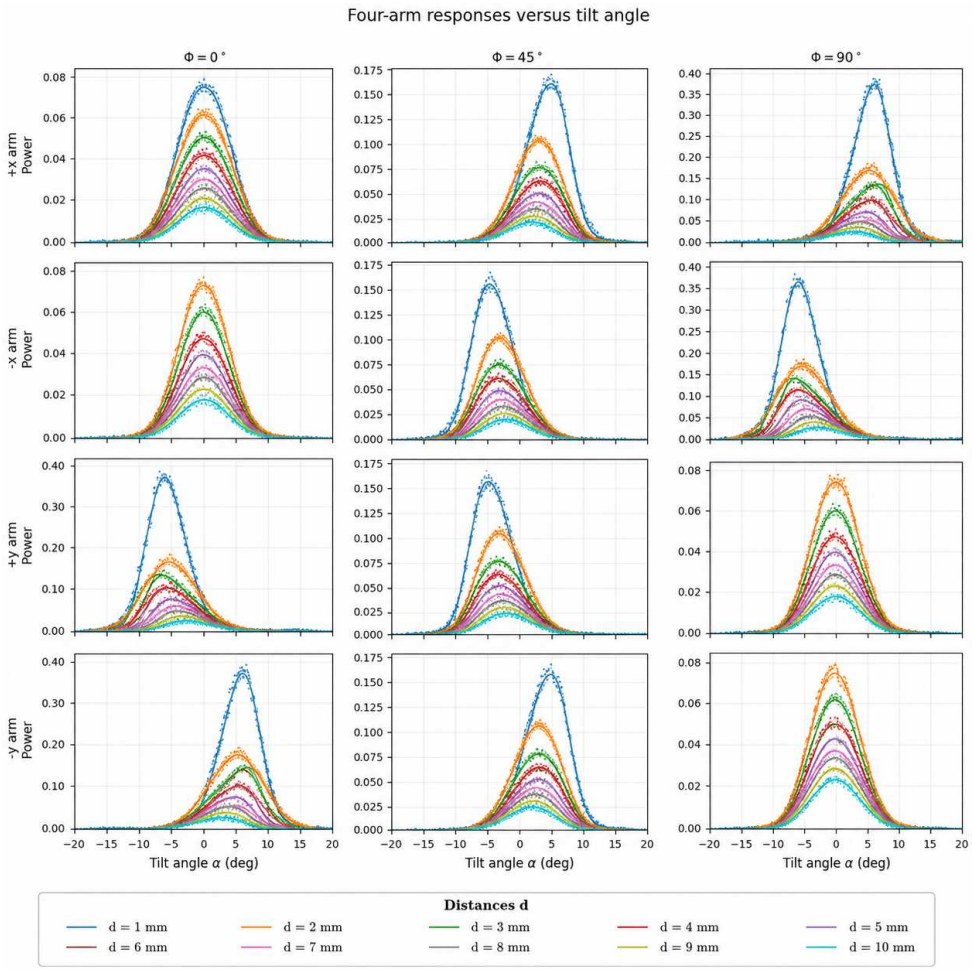



**Fig. 5** Response of the four directional arms as a function of tilt angle for ten distances between 1 mm and 10 mm. Columns correspond to $\Phi = 0°$, $45°$ and $90°$, while rows correspond to the $+x$, $-x$, $+y$ and $-y$ arms. Solid curves denote the ideal model and dashed curves denote measured responses. The pointwise standard deviation varied with the operating point, with a nominal mean of approximately $4.5 \times 10^{-3}$ a.u.

governed by the radial distribution of the optical field. The dimensionless ring-power ratio

$$\eta(d, \alpha, \Phi) = \frac{P_{\text{out}}(d, \alpha, \Phi)}{P_{\text{in}}(d, \alpha, \Phi)} \tag{4.4}$$

therefore suppresses common multiplicative variations while preserving the redistribution of optical power between the two radii[37–40].

Figure 7 summarizes this behaviour. Plot (a) represents $\eta$ as a function of distance for $\alpha = -10°, -8°, \ldots, 10°$ at $\Phi = 0°$. Because the ideal ring response is even in $\alpha$, the curves for positive and negative angles of equal magnitude coincide and are grouped as $\alpha = \pm 2°, \pm 4°, \ldots, \pm 10°$. Plot (b) represents the same ratio for $\Phi = 0°, 15°, \ldots, 90°$ at

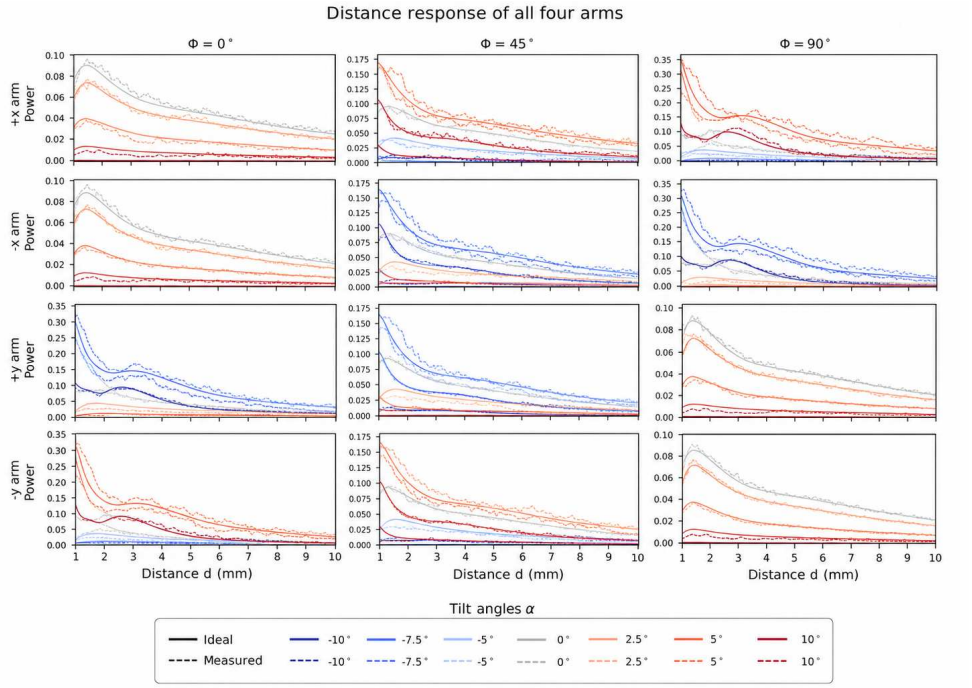



**Fig. 6** Distance response of the four directional arms for three tilt-axis azimuths and several tilt angles. Rows correspond to the $+x$, $-x$, $+y$ and $-y$ arms, while columns correspond to $\Phi = 0°$, $45°$ and $90°$. Solid curves denote the ideal model and dashed curves denote measured responses. The pointwise standard deviation varied with the operating point, with a nominal mean of approximately $4.9 \times 10^{-3}$ a.u.

$\alpha = 0°$. Solid curves correspond to the ideal model and dashed curves to measured-like responses.

The left plot shows that the ratio changes markedly with distance and tilt magnitude. Tilting the target displaces the reflected spot radially relative to the two receiving rings, changing the fraction of light intercepted by the outer ring with respect to the inner one. The six clearly separated families correspond to $|\alpha| = 0°, 2°, 4°, 6°, 8°$ and $10°$. The ideal response is exactly even in $\alpha$ for the inversion-symmetric ring geometry, whereas the measured curves show only small stochastic deviations around the common ideal response. By contrast, the right plot shows that the dependence on the tilt-axis azimuth is negligible when $\alpha = 0°$. The curves of the model coincide because the spot is centred and the ring geometry is rotationally symmetric. The measured curves remain tightly grouped, with only small differences caused by independent channel perturbations. Consequently, the ratio contains strong information about $d$ and $|\alpha|$ but almost no information about $\Phi$.

This separation of roles is central to the proposed sensor. The cross arms provide directional information, whereas the rings provide an approximately azimuth-invariant radial observable. Their combination reduces the ambiguity that would arise

from using either subsystem alone and provides the physical basis for simultaneous reconstruction of distance, tilt magnitude and tilt-axis azimuth.

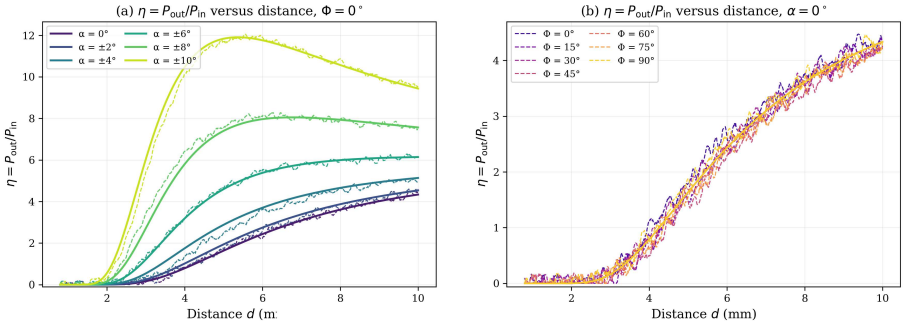



**Fig. 7** Ring-power ratio $\eta = P_{\text{out}}/P_{\text{in}}$ as a function of distance. (a) Responses for $\alpha = 0°, \pm 2°, \pm 4°, \pm 6°, \pm 8°$ and $\pm 10°$ with $\Phi = 0°$; the ideal responses for opposite signs coincide. (b) Responses for tilt-axis azimuths from $0°$ to $90°$ in steps of $15°$ with $\alpha = 0°$. The solid curves represent the model and the dashed curves represent the measurements. The pointwise standard deviation varied with the operating point, with a nominal mean of approximately $1.2 \times 10^{-2}$.

## 4.4 Linearized observables for simultaneous reconstruction

The most useful observables are not the raw powers but the logarithmic ratios

$$L_x = \ln\left(\frac{P_{+x}}{P_{-x}}\right), \qquad L_y = \ln\left(\frac{P_{+y}}{P_{-y}}\right), \qquad Q = \ln\left(\frac{P_{\text{out}}}{P_{\text{in}}}\right), \tag{4.5}$$

combined with

$$L_{\text{mag}} = \sqrt{L_x^2 + L_y^2}. \tag{4.6}$$

The log-ratio transformation cancels common multiplicative factors such as source power, mirror reflectivity and global gain, and converts opposite-arm asymmetry into an approximately linear angular variable. For moderate tilt, the first-order model gives (see Section A.8 in the Appendix)

$$L_x \approx A(d, \alpha) \sin \Phi, \qquad L_y \approx -A(d, \alpha) \cos \Phi, \tag{4.7}$$

where $A(d, \alpha)$ is a scalar amplitude determined by distance, tilt magnitude and effective arm position. This relation explains why $\text{atan2}(L_x, -L_y)$ estimates $\Phi$, and why $L_{\text{mag}}$ is mainly sensitive to $|\alpha|$ and $d$ but only weakly to $\Phi$.

Figures 8, 9 and 10 show these four observables for representative distances and three tilt-axis azimuths. The $L_x$ and $L_y$ curves rotate their sensitivity with $\Phi$: for $\Phi = 0°$ the $x$ log-ratio is nearly zero and the $y$ log-ratio carries most angular information, whereas for $\Phi = 90°$ the opposite occurs. For $\Phi = 45°$ both log-ratios contribute. The slopes decrease with increasing distance, so shorter distances are more angularly sensitive. Very short distances, however, may also be more affected by mechanical admissibility and low-power regions.

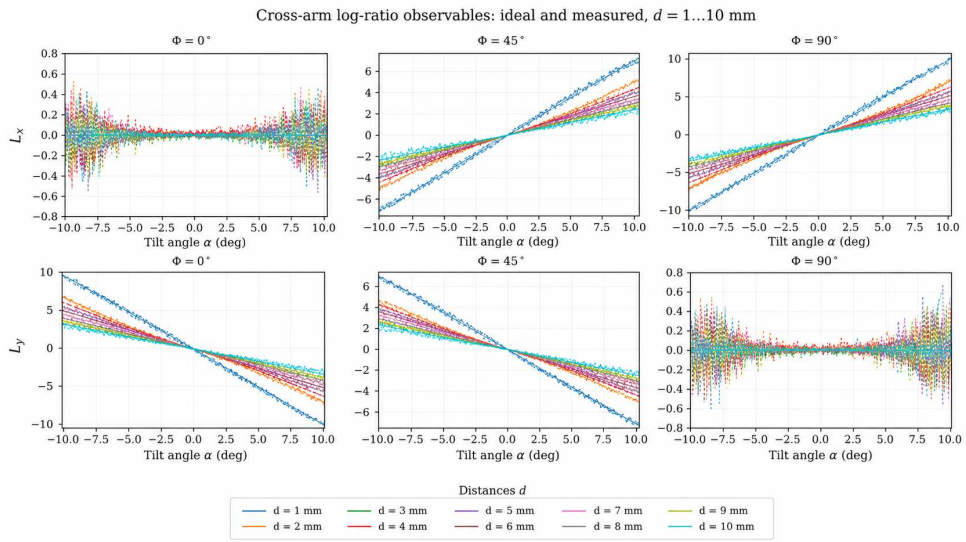



**Fig. 8** Directional observables arranged in two rows and three columns. Top row: $L_x = \ln(P_{+x}/P_{-x})$ versus tilt angle for $\Phi = 0°$, $45°$, and $90°$. Bottom row: $L_y = \ln(P_{+y}/P_{-y})$ for the same three tilt-axis azimuths. The solid curves represent the model and the dashed curves represent the measurements. The distance color code is summarized below the plots. The pointwise standard deviation varied with the operating point, with a nominal mean of approximately $5.0 \times 10^{-2}$.

The ring observable $Q$ is almost independent of $\Phi$ because the rings are nearly azimuthally symmetric. It is also approximately even in $\alpha$, and therefore cannot determine the sign of the tilt. Its role is to provide radial information that helps separate distance and tilt magnitude. In contrast, $L_{\mathrm{mag}}$ summarizes the arm imbalance independently of azimuth; it is close to zero at $\alpha = 0$ and increases approximately linearly with $|\alpha|$ when $d$ is known.

For $d = 1$ mm in Fig. 9, the response around $\alpha = 0°$ becomes especially noisy because $P_{\mathrm{out}}$ is extremely small there. As a result, the ratio $P_{\mathrm{out}}/P_{\mathrm{in}}$ is dominated by perturbations and the corresponding measured curve is not reliable in the central interval, approximately between $-2.5°$ and $2.5°$. By contrast, all curves in Fig. 10 pass through zero at $\alpha = 0°$ because the centred reflected spot gives $P_{+x} = P_{-x}$ and $P_{+y} = P_{-y}$; consequently, $L_x = L_y = 0$ and $L_{\mathrm{mag}} = 0$.

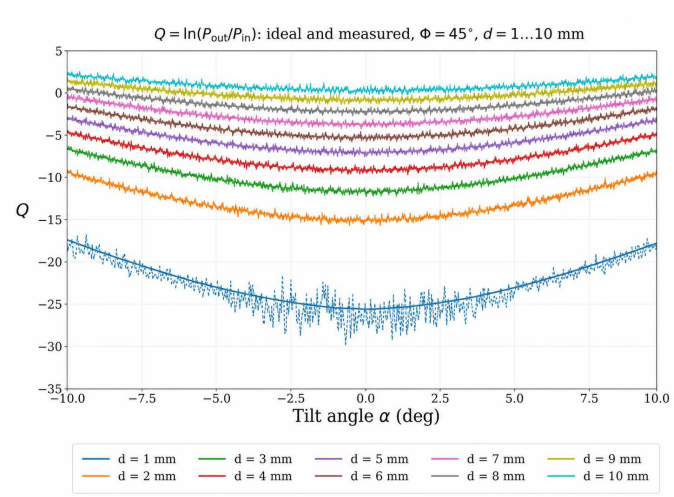



**Fig. 9** Ring observable $Q = \ln(P_{\text{out}}/P_{\text{in}})$ versus tilt angle for $\Phi = 45°$. The solid curves represent the model and the dashed curves represent the measurements. Its weak dependence on $\Phi$ makes it useful for radial distance–tilt discrimination rather than for signed angle estimation. The pointwise standard deviation varied with the operating point, with a nominal mean of approximately 0.25 for $d = 2, \ldots, 10$ mm, increasing in the low-signal region of the $d = 1$ mm curve.

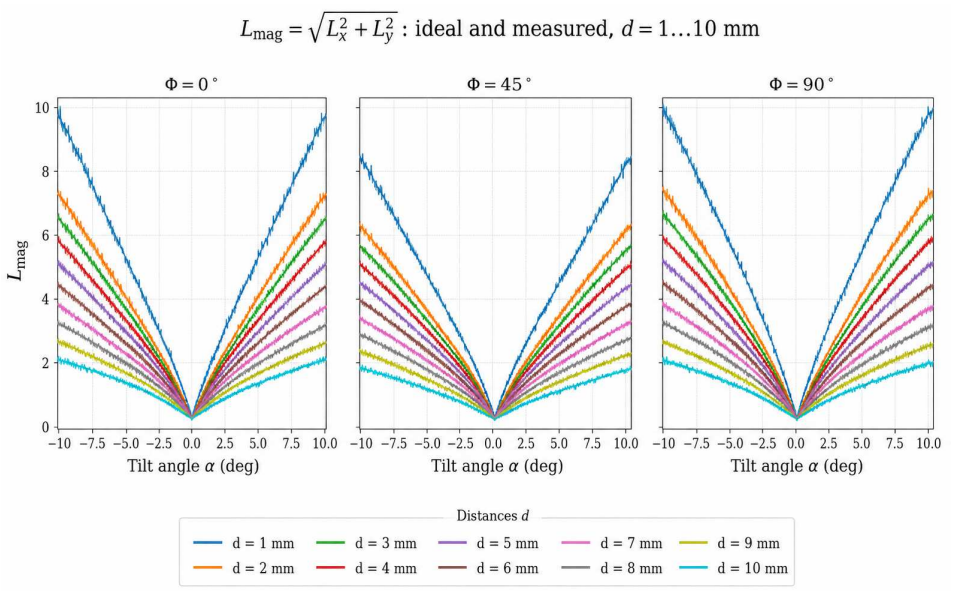



**Fig. 10** Magnitude observable $L_{\text{mag}} = \sqrt{L_x^2 + L_y^2}$ versus tilt angle. This observable is nearly independent of the tilt-axis azimuth and provides a compact measure of tilt magnitude when the distance is known or calibrated. The solid curves represent the model and the dashed curves represent the measurements. The pointwise standard deviation varied with the operating point, with a nominal mean of approximately $5.0 \times 10^{-2}$.

The combined interpretation is as follows. The pair $(L_x, L_y)$ provides the directional information needed to estimate $\Phi$. Once $\Phi$ is known, the projected observable $L_\parallel$ gives the signed response along the tilt direction, while $Q$ provides radial information. The pair $(L_\parallel, Q)$ is therefore the natural reduced representation for estimating $d$ and $\alpha$. The six-power vector remains necessary for the final refinement because it uses all available information and avoids relying on a single non-monotonic channel. Relative to conventional bundle OFDSs, the OFLADS adds two-dimensional angular observability while retaining scalar intensity interrogation and a passive sensing head. Unlike interferometric, spectral or image-based multi-axis approaches, the three unknowns are encoded by the complementary directional and radial power distributions of one bundle and recovered through the model-based inversion.

# 5 Reconstruction examples

This section illustrates the complete reconstruction pipeline with five measured examples. The goal is to show how the six measured powers are transformed into a practical estimate of $\Phi$, $d$ and $\alpha$.

## 5.1 Reconstruction procedure

The reconstruction strategy separates directional and radial information. First, the four cross-arm powers are transformed into the opposite-arm logarithmic ratios

$$L_x = \ln\left(\frac{P_{+x}}{P_{-x}}\right), \qquad L_y = \ln\left(\frac{P_{+y}}{P_{-y}}\right), \tag{5.1}$$

and the direct azimuth estimate is obtained as

$$\widehat{\Phi}_0 = \operatorname{atan2}(L_x, -L_y). \tag{5.2}$$

Once $\widehat{\Phi}_0$ has been estimated, the directional response is projected along the inferred tilt direction,

$$L_\parallel = L_x \sin\widehat{\Phi}_0 - L_y \cos\widehat{\Phi}_0, \tag{5.3}$$

and combined with the ring log-ratio

$$Q = \ln\left(\frac{P_{\mathrm{out}}}{P_{\mathrm{in}}}\right). \tag{5.4}$$

The measured pair $(L_\parallel, Q)$ is then compared with the calibrated full-model map

$$(d, \alpha) \longmapsto \big(L_\parallel(d, \alpha; \widehat{\Phi}_0), Q(d, \alpha; \widehat{\Phi}_0)\big), \tag{5.5}$$

which yields the initial estimate $(d_0, \alpha_0)$. Finally, the complete six-power vector

$$\mathbf{P} = [P_{+x}, P_{-x}, P_{+y}, P_{-y}, P_{\mathrm{in}}, P_{\mathrm{out}}]^{\mathsf{T}} \tag{5.6}$$

is used in a nonlinear refinement. The operational sequence is therefore explicit: (i) $L_x$ and $L_y$ provide the initializer $\widehat{\Phi}_0$; (ii) $L_\parallel$ and $Q$ locate the nearest point of the calibrated map and provide $(d_0, \alpha_0)$; and (iii) a joint six-power fit starts from $(d_0, \alpha_0, \widehat{\Phi}_0)$ and refines $d$, $\alpha$ and $\Phi$ simultaneously.

The calibration map was tabulated on a regular grid with $\Delta d = 0.1$ mm over $1 \le d \le 10$ mm, $\Delta\alpha = 0.25^\circ$ over $-10^\circ \le \alpha \le 10^\circ$, and $\Delta\Phi = 1^\circ$ over $0^\circ \le \Phi \le 90^\circ$. Trilinear interpolation was used between grid nodes. The map-distance normalization used $s_L = 10.0$ and $s_Q = 30.5$.

The forward model is evaluated with unit gain. The measured powers may differ from it by a single common scale $C$,

$$P_i^{\mathrm{meas}} \approx C\, P_i^{\mathrm{mod}}(d, \alpha, \Phi), \qquad c = \ln C,$$

where $C$ represents the same global optical–electronic scale denoted by $G$ in the forward model; it is not an additional gain. The weighted logarithmic residual is

$$\chi^2(d, \alpha, \Phi, c) = \sum_{i=1}^{6} w_i \left[\ln P_i^{\mathrm{meas}} - c - \ln P_i^{\mathrm{mod}}(d, \alpha, \Phi)\right]^2. \tag{5.7}$$

For each candidate $(d, \alpha, \Phi)$, the optimal log-gain is obtained analytically as

$$\widehat{c}(d, \alpha, \Phi) = \frac{\sum_{i=1}^{6} w_i \left[\ln P_i^{\mathrm{meas}} - \ln P_i^{\mathrm{mod}}(d, \alpha, \Phi)\right]}{\sum_{i=1}^{6} w_i}.$$

Thus, $C$ is removed from the numerical search while its effect remains represented in the residual.

The coefficients $w_i$ specify the relative importance of the six channels. Equal weights, $w_i = 1$, were used because the channels were gain-calibrated and acquired through equivalent detection chains. The joint fit minimizes $\chi^2(d, \alpha, \Phi, \widehat{c})$ within the grid bounds and the mechanical-admissibility constraint. Candidates with $g_{\mathrm{mech}} = 0$ are discarded before evaluating the logarithms. The solver stops when both the relative change in $\chi^2$ and

$$\max\left(\frac{|\Delta d|}{1\ \mathrm{mm}}, \frac{|\Delta\alpha|}{1^\circ}, \frac{|\Delta\Phi|}{1^\circ}\right)$$

are below $10^{-8}$, or after 500 model evaluations. The refined solution is retained only when it decreases $\chi^2$ relative to the map-initialized state; otherwise the map estimate is kept. Because $\chi^2$ measures six-channel optical consistency, this safeguard does not imply that every component-wise parameter error must decrease.

## 5.2 Measured examples

Five representative operating points were selected to test the complete inverse procedure over different combinations of distance, tilt magnitude and tilt-axis azimuth. Figure 11 shows the corresponding measured response curves. Each row represents one test case and each column one of the six optical channels. The highlighted point

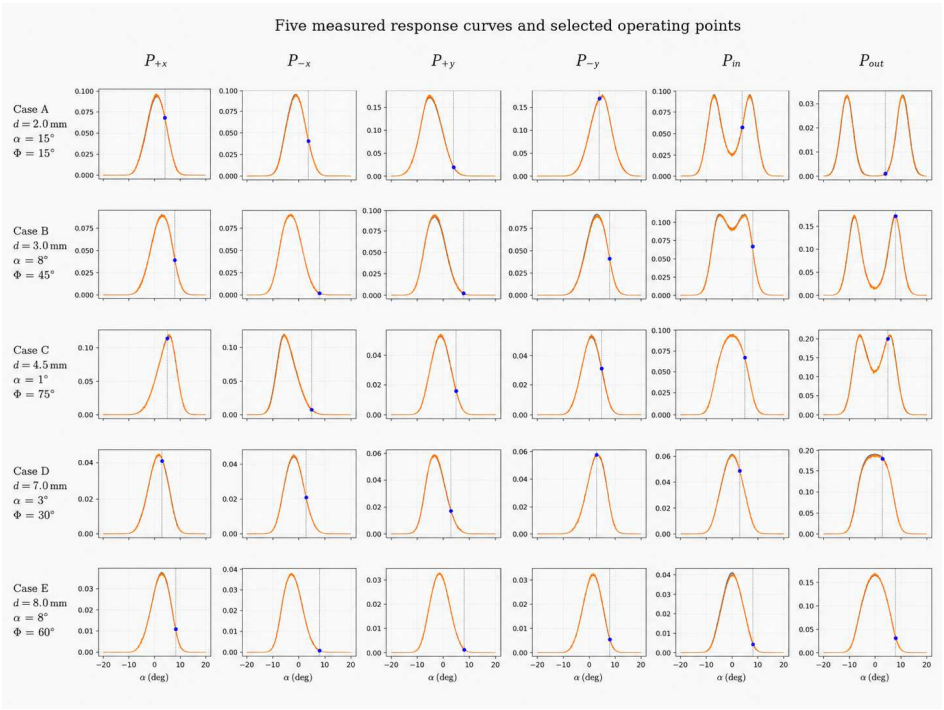



**Fig. 11** Measured response curves and selected measurement points used for the inverse examples. The five rows correspond to cases A–E, and the six clearly labelled columns correspond to $P_{+x}$, $P_{-x}$, $P_{+y}$, $P_{-y}$, $P_{\mathrm{in}}$ and $P_{\mathrm{out}}$. The highlighted point in each plot is the measured value supplied to the reconstruction algorithm.

in each plot is the measured value supplied to the reconstruction algorithm. The measured curves remain close to the corresponding reference model curves, confirming that the model reproduces the measured results.

## 5.3 Reconstruction accuracy

Table 4 summarizes the numerical reconstruction errors for the five measured points. The direct azimuth estimate initializes the final joint fit. The map estimate refers to the calibrated $(L_{\parallel}, Q)$ inversion, whereas the final estimate is obtained from the joint six-power refinement of $d$, $\alpha$ and $\Phi$.

The reported mean absolute reconstruction errors combine model mismatch, experimental perturbations and the limited sensitivity of the inverse reconstruction.

Although only five examples are shown for reasons of space, they were selected to span distinct combinations of $d$, $\alpha$ and $\Phi$, and the associated errors are representative of the reconstruction performance observed across the evaluated operating range.

All five final solutions satisfy the working-range, admissibility and residual-decrease criteria. The calibrated map provides a robust initial estimate, and the joint six-power refinement improves the agreement between the complete measured and modeled power vectors. Since the optimized quantity is the optical residual, the error of an

**Table 4** Numerical reconstruction errors for the five measured points. The final estimate corresponds to the joint six-power refinement of $d$, $\alpha$ and $\Phi$.

| Case | $d_{\text{true}}$ mm | $\alpha_{\text{true}}$ deg | $\Phi_{\text{true}}$ deg | $\widehat{\Phi}$ deg | $\Phi$ err. % | Map $d$ err. % | Map $\alpha$ err. % | Final $d$ err. % | Final $\alpha$ err. % |
|---|---|---|---|---|---|---|---|---|---|
| A | 2.0 | 4.0 | 15.0 | 14.27 | −4.87 | 2.50 | 0.00 | 1.56 | −0.86 |
| B | 3.0 | 8.0 | 45.0 | 45.87 | 1.93 | 3.33 | −4.69 | 0.40 | −2.62 |
| C | 4.5 | 5.0 | 75.0 | 75.58 | 0.77 | −1.11 | 0.00 | −0.21 | −0.44 |
| D | 7.0 | 3.0 | 30.0 | 28.26 | −5.80 | 0.00 | −4.17 | −0.54 | −4.65 |
| E | 9.0 | 8.0 | 60.0 | 59.55 | −0.75 | −2.22 | −3.13 | 5.44 | 1.73 |

individual parameter can occasionally increase even when the overall six-channel fit improves.

The largest final distance error occurs for case E, where the target is far from the bundle and the tilt magnitude is high. This behaviour is consistent with the weaker conditioning of the distance–tilt inversion in the large-distance/high-tilt region: the power distributions vary more slowly with distance and different parameter combinations become less distinguishable. Case D exhibits the largest final tilt error. In that case the tilt magnitude is small, the opposite-arm imbalance is correspondingly weak, and the recovered angular magnitude becomes more sensitive to perturbations.

These results support the proposed workflow: the calibrated map provides a physically meaningful starting point, while the six-power fit gives the final estimate.

# 6 Conclusions

This work introduces the OFLADS for simultaneous estimation of the target distance $d$, tilt magnitude $\alpha$ and tilt-axis azimuth $\Phi$. The four directional cross arms and two concentric receiving rings encode complementary directional and radial information in six reflected-power measurements, allowing a single passive sensing head and conventional photodetection electronics to address a three-parameter problem that conventional bundle OFDSs do not resolve.

The principal contribution is the combined development of the OFLADS geometry, a physically based forward model and a structured inverse procedure for simultaneously inferring the three geometric parameters $d$, $\alpha$ and $\Phi$. The model resolves the individual receiving-fiber contributions and includes finite-core coupling, numerical-aperture attenuation, mechanical admissibility and an unknown global gain. The reconstruction first estimates $\Phi$ from opposite-arm logarithmic ratios, obtains an initial $(d, \alpha)$ estimate from a calibrated map, and then jointly refines $d$, $\alpha$ and $\Phi$ with the complete six-power vector while eliminating the common gain analytically.

Across the five validation cases, the mean absolute reconstruction errors were 1.63% for distance, 2.06% for tilt magnitude and 0.87° for tilt-axis azimuth; the corresponding maximum absolute errors were 5.44%, 4.65% and 1.74°. These results support the feasibility of a compact and potentially low-cost three-parameter sensor for many industrial applications requiring simultaneous non-contact monitoring of distance, tilt magnitude and tilt-axis orientation, including positioning, alignment and robotic metrology tasks, while also identifying large-distance/high-tilt operation as the least favorable region because of weaker inverse-problem conditioning. Furthermore, the distinctive

directional–radial architecture of the OFLADS may enable sensing applications that are not readily achievable with conventional fiber-bundle configurations.

# Declarations

**Funding.** This work was supported in part by MICIU/AEI under Grant PID2024-155582OB-C31, Grant PID2024-158310NB-I00, and Grant PDC2025-165025-C21; in part by the "ERDF a Way of Making Europe" and "European Union Next GenerationEU/PRTR"; in part by the Gobierno Vasco/Eusko Jaurlaritza under Grant IT1829-26, Grant ELKARTEK KK 2025/00058, and Grant ELKARTEK KK-2025/00074; and in part by the University of the Basque Country UPV/EHU under Grant Translight.

**Competing interests.** The authors declare no competing interests.

**Ethics approval and consent to participate.** Not applicable.

**Consent for publication.** Not applicable.

**Data availability.** The data that support the findings of this study are available from the corresponding author, upon reasonable request.

**Materials availability.** Not applicable.

**Code availability.** Not applicable.

**Author contributions.** J.Z. conceived the idea and supervised the project. G.Z., G.D., and O.A. performed the experiments. G.A., G.D., G.Z., and J.A. analyzed the data. G.Z. wrote the manuscript with input from all authors.

# Appendix A Complete model of the OFLADS

This appendix summarizes the mathematical model used to compute the optical power collected by each receiving collection of the heptafurcated bundle, and the inverse procedure used to recover the target distance $d$, the tilt magnitude $\alpha$, and the tilt-axis angle $\Phi$ from the measured powers.

## A.1 Geometry and sign convention

The bundle face is placed at the plane $z = 0$, and the central transmitting fiber (TF) is located at the origin. The mirror centre is at axial distance $d$ from the bundle face and is tilted by an angle $\alpha$ about an in-plane axis whose azimuth is $\Phi$. The in-plane tilt-axis unit vector is

$$\mathbf{u}_\Phi = (\cos\Phi, \sin\Phi, 0). \tag{A.1}$$

According to specular reflection, the axis of the reflected beam is rotated by $2\alpha$. Its intersection with the bundle plane is displaced from the origin by the vector

$$\mathbf{s}(d, \alpha, \Phi) = S(d, \alpha)(\sin\Phi, -\cos\Phi), \qquad S(d, \alpha) = d\tan(2\alpha). \tag{A.2}$$

A receiving fiber whose centre is located at polar coordinates $(R, \psi)$ has Cartesian position

$$\mathbf{r}_{R,\psi} = R(\cos\psi, \sin\psi). \tag{A.3}$$

The squared distance between the receiving-fiber centre and the centre of the reflected Gaussian spot is therefore

$$\begin{aligned}\rho^2(R, \psi; d, \alpha, \Phi) &= |\mathbf{r}_{R,\psi} - \mathbf{s}(d, \alpha, \Phi)|^2 \\ &= R^2 + S^2(d, \alpha) + 2RS(d, \alpha)\sin(\psi - \Phi).\end{aligned} \tag{A.4}$$

This expression is the geometrical core of the model. It shows that $d$ and $\alpha$ determine the magnitude of the lateral spot displacement, while $\Phi$ determines how that displacement is projected onto each receiving collection.

## A.2 Single-fiber received power

Let a receiving fiber have core radius $r$, radial position $R$, and azimuth $\psi$. The exact collected power can be written as an overlap integral over the circular core area $\Omega_r$ of the receiving fiber,

$$P^{\text{exact}}_{R,\psi,r}(d, \alpha, \Phi) = G\, g_{\text{tot}}(d, \alpha; R_T) \iint_{\Omega_r} I(x, y; d, \alpha, \Phi)\, dx\, dy, \tag{A.5}$$

where $G$ is the single common optical–electronic scale factor. It includes the product of emitted power and target reflectivity, fiber losses, detector responsivity and electronic gain. The factor $g_{\text{tot}}$ accounts for numerical-aperture acceptance and mechanical admissibility, as described below. The reflected irradiance at the bundle plane is modelled as a tilted Gaussian field,

$$I(x, y; d, \alpha, \Phi) \propto \exp\Big[-B(d, \alpha)\,|(x, y) - \mathbf{s}(d, \alpha, \Phi)|^2\Big]. \tag{A.6}$$

The Gaussian decay coefficient is

$$B(d, \alpha) = \frac{2\cos^2(2\alpha)}{d^2[1 + \cos(2\alpha)]^2 \tan^2\theta_0}, \tag{A.7}$$

where $\theta_0$ is the emission half-angle of the transmitting fiber. For fast evaluation, the integral is approximated by the mean-value expression[39]

$$P_{R,\psi,r}(d, \alpha, \Phi) = G\, g_{\text{tot}}(d, \alpha; R_T) K(d, \alpha; r) \exp\big[-B(d, \alpha)\rho^2(R, \psi; d, \alpha, \Phi)\big]. \tag{A.8}$$

The corrected finite-core factor $K$ is

$$K(d, \alpha; r) = \frac{4r\cos^2(2\alpha)}{\pi d[1 + \cos(2\alpha)]\tan\theta_0} \operatorname{erf}\left[\frac{2r\cos^2\alpha}{d[1 + \cos(2\alpha)]\tan\theta_0}\right]. \tag{A.9}$$

The factor $K$ is purely geometrical; all common optical and electronic scale terms are included once, in $G$. This expression is the forward model used for each individual receiving fiber. If maximum accuracy is required, the exact overlap integral can be evaluated numerically instead.

## A.3 Numerical-aperture and mechanical admissibility

The previous expression describes the geometrical overlap between the reflected irradiance and the receiving fiber core. However, not all geometrically incident light is accepted by the fiber. The receiving fiber only accepts light within its acceptance cone, whose half-angle is

$$\theta_{\mathrm{NA}} = \arcsin(\mathrm{NA}). \tag{A.10}$$

For a tilted target, the reflected cone is shifted angularly. A practical way to include this effect is to introduce a numerical-aperture gate. Let

$$\alpha_{\mathrm{NA}} = \theta_{\mathrm{NA}} - \theta_0. \tag{A.11}$$

Then

$$g_{\mathrm{NA}}(\alpha) = \begin{cases} 1, & |\alpha| \le \alpha_{\mathrm{NA}}, \\ \exp\left[-\left(\dfrac{|\alpha| - \alpha_{\mathrm{NA}}}{\sigma_{\mathrm{NA}}}\right)^2\right], & |\alpha| > \alpha_{\mathrm{NA}}, \end{cases} \tag{A.12}$$

where $\sigma_{\mathrm{NA}}$ controls the smoothness of the transition; $\sigma_{\mathrm{NA}} = 5^\circ$ was used. Equivalently, the same factor can be written as

$$g_{\mathrm{NA}}(\alpha) = \begin{cases} 1, & |\alpha| + \theta_0 \le \theta_{\mathrm{NA}}, \\ \exp\left[-\left(\dfrac{|\alpha| + \theta_0 - \theta_{\mathrm{NA}}}{\sigma_{\mathrm{NA}}}\right)^2\right], & |\alpha| + \theta_0 > \theta_{\mathrm{NA}}. \end{cases} \tag{A.13}$$

Both forms are equivalent if $\alpha_{\mathrm{NA}} = \theta_{\mathrm{NA}} - \theta_0$, although the second form makes the physical meaning clearer: the reflected cone is progressively attenuated when the emission half-angle plus the target tilt exceeds the receiving acceptance half-angle.

A second gate is required because not every mathematically defined tilt is mechanically possible. If $R_T$ is the mechanical outer radius of the bundle tip or ferrule, the mirror would contact the bundle edge when

$$|\alpha| > \alpha_{\max}(d; R_T), \qquad \alpha_{\max}(d; R_T) = \arctan\left(\frac{d}{R_T}\right). \tag{A.14}$$

Therefore,

$$g_{\mathrm{mech}}(d, \alpha; R_T) = H\left[\arctan\left(\frac{d}{R_T}\right) - |\alpha|\right], \tag{A.15}$$

where $H$ is the Heaviside step function. The global admissibility factor is then

$$g_{\mathrm{tot}}(d, \alpha; R_T) = g_{\mathrm{NA}}(\alpha) g_{\mathrm{mech}}(d, \alpha; R_T). \tag{A.16}$$

This factor is included in every fiber channel of the bundle model. Since it is common to all channels, it cancels from the power ratios; its role is to represent absolute attenuation and to delimit the admissible domain. Any candidate with $g_{\mathrm{mech}} = 0$ is rejected before evaluating a logarithm.

## A.4 Heptafurcated bundle model

The heptafurcated bundle contains four directional arms and two concentric receiving rings. The four arm azimuths are

$$\psi_{+x} = 0, \qquad \psi_{-x} = \pi, \qquad \psi_{+y} = \frac{\pi}{2}, \qquad \psi_{-y} = \frac{3\pi}{2}. \tag{A.17}$$

Each arm contains three fibers placed at radii $R_i$ with core radii $r_i$. For the geometry used in the simulations,

$$(R_i, r_i) = (0.25, 0.11),\ (0.70, 0.11),\ (1.26, 0.22)\ \text{mm}. \tag{A.18}$$

The power collected by an arm at azimuth $\psi_a$ is

$$P_a(d, \alpha, \Phi) = G \sum_{i=1}^{3} g_{\mathrm{tot}}(d, \alpha; R_T) K_i(d, \alpha; r_i) \exp\!\left[-B(d, \alpha)\rho^2(R_i, \psi_a; d, \alpha, \Phi)\right]. \tag{A.19}$$

For the ring channels, $\Psi_{\mathrm{in}} = \{(2i-1)\pi/8 : i = 1, \ldots, 8\}$ and $\Psi_{\mathrm{out}} = \{(2i-1)\pi/12 : i = 1, \ldots, 12\}$ are the azimuth sets of the inner and outer rings, respectively, excluding the cardinal directions occupied by the cross arms. Then

$$P_{\mathrm{in}}(d, \alpha, \Phi) = G \sum_{\psi \in \Psi_{\mathrm{in}}} g_{\mathrm{tot}}(d, \alpha; R_T) K(d, \alpha; r_{\mathrm{in}}) \exp\!\left[-B(d, \alpha)\rho^2(R_{\mathrm{in}}, \psi; d, \alpha, \Phi)\right], \tag{A.20}$$

$$P_{\mathrm{out}}(d, \alpha, \Phi) = G \sum_{\psi \in \Psi_{\mathrm{out}}} g_{\mathrm{tot}}(d, \alpha; R_T) K(d, \alpha; r_{\mathrm{out}}) \exp\!\left[-B(d, \alpha)\rho^2(R_{\mathrm{out}}, \psi; d, \alpha, \Phi)\right]. \tag{A.21}$$

For an azimuthally dense and perfectly symmetric ring, the dependence on $\Phi$ becomes weak.

The six powers used in the reconstruction of $d$, $\alpha$ and $\Phi$ are

$$\mathbf{P} = [P_{+x}, P_{-x}, P_{+y}, P_{-y}, P_{\mathrm{in}}, P_{\mathrm{out}}]^{\mathsf{T}}. \tag{A.22}$$

## A.5 Direct estimation of the tilt-axis angle

The four directional arms provide the most direct information about the tilt-axis azimuth. Define the opposite-arm log-ratios:

$$L_x = \ln\!\left(\frac{P_{+x}}{P_{-x}}\right), \qquad L_y = \ln\!\left(\frac{P_{+y}}{P_{-y}}\right). \tag{A.23}$$

In numerically stable form, these can be computed from normalized differential ratios,

$$D_x = \frac{P_{+x} - P_{-x}}{P_{+x} + P_{-x}}, \qquad D_y = \frac{P_{+y} - P_{-y}}{P_{+y} + P_{-y}}, \tag{A.24}$$

using the exact identities

$$L_x = 2\,\mathrm{atanh}(D_x), \qquad L_y = 2\,\mathrm{atanh}(D_y). \tag{A.25}$$

The first estimate of the tilt-axis angle is

$$\widehat{\Phi}_0 = \mathrm{atan2}(L_x, -L_y). \tag{A.26}$$

This estimator is not an exact identity of the full three-fiber arm model, because each arm is a sum of fibers at different radii. However, it is a very effective direct estimator of $\Phi$. It becomes ill-conditioned only when $\alpha \approx 0$, because then $L_x \approx L_y \approx 0$ and the tilt axis is physically undefined.

The magnitude of the directional imbalance is

$$L_{\mathrm{mag}} = \sqrt{L_x^2 + L_y^2}. \tag{A.27}$$

A small value of $L_{\mathrm{mag}}$ should be used as a warning that the estimated $\widehat{\Phi}_0$ is unreliable.

## A.6 Reconstruction of distance and tilt after estimating $\Phi$

Once $\widehat{\Phi}_0$ has been obtained, the arm information is projected along the estimated tilt direction:

$$L_{\parallel} = L_x \sin\widehat{\Phi}_0 - L_y \cos\widehat{\Phi}_0. \tag{A.28}$$

This scalar observable keeps the sign of the tilt angle. The ring observable is

$$Q = \ln\!\left(\frac{P_{\mathrm{out}}}{P_{\mathrm{in}}}\right). \tag{A.29}$$

The pair $(L_{\parallel}, Q)$ is used to obtain an initial estimate of $(d, \alpha)$.

For each candidate pair $(d, \alpha)$, with $\Phi$ fixed at $\widehat{\Phi}_0$, the model gives

$$\mathcal{M}_{\widehat{\Phi}_0}(d,\alpha) = \left[L_{\parallel}^{\mathrm{mod}}(d,\alpha;\widehat{\Phi}_0), Q^{\mathrm{mod}}(d,\alpha;\widehat{\Phi}_0)\right]^{\mathsf{T}}. \tag{A.30}$$

The initial estimate is obtained from the calibrated-map minimization

$$(d_0,\alpha_0) = \arg\min_{d,\alpha}\left\{\left[\frac{L_{\parallel}^{\mathrm{meas}} - L_{\parallel}^{\mathrm{mod}}(d,\alpha;\widehat{\Phi}_0)}{s_L}\right]^2 + \left[\frac{Q^{\mathrm{meas}} - Q^{\mathrm{mod}}(d,\alpha;\widehat{\Phi}_0)}{s_Q}\right]^2\right\}, \tag{A.31}$$

The map was tabulated on the regular grid $d = 1.0{:}0.1{:}10.0$ mm, $\alpha = -10°{:}0.25°{:}10°$ and $\Phi = 0°{:}1°{:}90°$, and evaluated by trilinear interpolation. The scaling values were $s_L = 10.0$ and $s_Q = 30.5$. The minimization is constrained by

$$d_{\min} \le d \le d_{\max}, \qquad |\alpha| \le \min\left(\alpha_{\text{work}}, \arctan\frac{d}{R_T}\right). \tag{A.32}$$

The calibrated map is the recommended first estimate because it is fast, physically interpretable, and robust.

## A.7 Six-power nonlinear refinement

The calibrated map compresses the six measured powers into two observables. The final estimator should use all six powers. Let

$$\mathbf{P}^{\text{meas}} = \left[P^{\text{meas}}_{+x}, P^{\text{meas}}_{-x}, P^{\text{meas}}_{+y}, P^{\text{meas}}_{-y}, P^{\text{meas}}_{\text{in}}, P^{\text{meas}}_{\text{out}}\right]^{\mathsf{T}} \tag{A.33}$$

and let $\mathbf{P}^{\text{mod}}(d, \alpha, \Phi)$ be computed from Eqs. (A.19)–(A.22) with unit gain. Since the absolute optical gain is generally unknown, the measured powers are modelled as

$$P^{\text{meas}}_i \approx C P^{\text{mod}}_i(d, \alpha, \Phi). \tag{A.34}$$

A convenient objective function is defined in the logarithmic domain:

$$\chi^2(d, \alpha, \Phi, c) = \sum_i w_i \left[\ln P^{\text{meas}}_i - c - \ln P^{\text{mod}}_i(d, \alpha, \Phi)\right]^2, \tag{A.35}$$

Here $C$ is the same common optical–electronic scale represented by $G$ in the forward model after the model has been evaluated with unit gain; $C$ is not an additional factor. The corresponding additive offset in the logarithmic domain is $c = \ln C$. The coefficients $w_i$ are non-negative channel weights. Equal weights, $w_i = 1$, were used for the six calibrated channels in the reported examples; inverse-variance weights may be substituted when channel-specific uncertainties are known. For every candidate $(d, \alpha, \Phi)$, the optimal log-gain is analytical:

$$\widehat{c}(d, \alpha, \Phi) = \frac{\sum_i w_i \left[\ln P^{\text{meas}}_i - \ln P^{\text{mod}}_i(d, \alpha, \Phi)\right]}{\sum_i w_i}. \tag{A.36}$$

Thus, the nonlinear problem can be solved without explicitly searching over $C$. The final joint estimate is

$$(\widehat{d}, \widehat{\alpha}, \widehat{\Phi}) = \arg\min_{d,\alpha,\Phi} \chi^2(d, \alpha, \Phi, \widehat{c}(d, \alpha, \Phi)), \tag{A.37}$$

initialized at $(d_0, \alpha_0, \widehat{\Phi}_0)$. The search uses $1 \le d \le 10$ mm, $-10° \le \alpha \le 10°$ and $0° \le \Phi \le 90°$, together with the mechanical-admissibility constraint. A bounded trust-region least-squares solver stops when both the relative objective-function change and

the normalized parameter step $\max(|\Delta d|/1\text{ mm}, |\Delta\alpha|/1^\circ, |\Delta\Phi|/1^\circ)$ are below $10^{-8}$, or after 500 model evaluations. The refined solution is retained only if it decreases $\chi^2$ relative to the map-initialized state; otherwise the map estimate is kept.

## A.8 First-order analytical model and effective radius

The full model above is the one used for quantitative reconstruction. A useful first-order model can be derived to interpret the arm log-ratios. For one arm at azimuth $\psi$, define

$$W_i(d,\alpha) = K_i(d,\alpha;r_i)\exp[-B(d,\alpha)R_i^2]. \tag{A.38}$$

The effective arm radius is the weighted mean

$$R_{\text{eff}}(d,\alpha) = \frac{\sum_{i=1}^{3} W_i(d,\alpha)R_i}{\sum_{i=1}^{3} W_i(d,\alpha)}. \tag{A.39}$$

Expanding the exact opposite-arm log-ratio to first order gives

$$L_\psi \approx -4B(d,\alpha)S(d,\alpha)R_{\text{eff}}(d,\alpha)\sin(\psi-\Phi). \tag{A.40}$$

Therefore,

$$L_x \approx 4BSR_{\text{eff}}\sin\Phi, \qquad L_y \approx -4BSR_{\text{eff}}\cos\Phi. \tag{A.41}$$

This explains why $\operatorname{atan2}(L_x, -L_y)$ estimates the tilt-axis angle $\Phi$ and why

$$L_{\text{mag}} \approx 4\,|B(d,\alpha)S(d,\alpha)R_{\text{eff}}(d,\alpha)|\,. \tag{A.42}$$

For small $\alpha$,

$$S(d,\alpha) \approx 2d\alpha, \qquad B(d,\alpha) \approx \frac{1}{2d^2\tan^2\theta_0}, \tag{A.43}$$

and hence

$$L_{\text{mag}} \approx \frac{4R_{\text{eff}}(d,0)}{d\tan^2\theta_0}|\alpha|. \tag{A.44}$$

These equations are useful for interpreting the sensor response and for building initial guesses.

## A.9 Practical reconstruction algorithm

Given the six measured powers

$$P_{+x}, P_{-x}, P_{+y}, P_{-y}, P_{\text{in}}, P_{\text{out}}, \tag{A.45}$$

the reconstruction algorithm is:

1. Correct dark offsets and channel gains. Accept the state only if every corrected channel satisfies $P_i > 5\sigma_{\text{dark},i}$; otherwise reject it before calculating logarithms.
2. Compute $D_x$, $D_y$, then $L_x = 2\,\operatorname{atanh}(D_x)$ and $L_y = 2\,\operatorname{atanh}(D_y)$.
3. Estimate the tilt-axis angle using Eq. (A.26). Reject or flag the estimate if $L_{\text{mag}}$ is below the noise threshold.

4. Compute $L_{\parallel}$ from Eq. (A.28) and $Q$ from Eq. (A.29).
5. Build or interpolate the calibrated map $\mathcal{M}_{\widehat{\Phi}_0}(d, \alpha)$ and obtain $(d_0, \alpha_0)$ from Eq. (A.31).
6. Starting from $(d_0, \alpha_0, \widehat{\Phi}_0)$, jointly refine $d$, $\alpha$ and $\Phi$ with the six-power inversion in Eq. (A.37), retaining the refined solution only when it reduces $\chi^2$.

# References


[1] Tao F, Qi Q. Digital twins and Industry 5.0: toward collaborative human–machine systems. Nature Publishing Group. 2021;8:14-26.

[2] Breque M, De Nul L, Petridis A. Industry 5.0: towards a sustainable, human-centric and resilient European industry. Luxembourg: Publications Office of the European Union; 2021. https://doi.org/10.2777/308407.

[3] Berkovic G, Shafir E. Optical methods for distance and displacement measurements. Adv Opt Photonics. 2012;4:441-71. https://doi.org/10.1364/AOP.4.000441.

[4] Shimamoto A, Tanaka K. Optical fiber bundle displacement sensor using an ac-modulated light source with subnanometer resolution and low thermal drift. Appl Opt. 1995;34(25):5854-60. https://doi.org/10.1364/AO.34.005854.

[5] Shimamoto A, Tanaka K. Geometrical analysis of an optical fiber bundle displacement sensor. Appl Opt. 1996;35(34):6767-74. https://doi.org/10.1364/AO.35.006767.

[6] Suganuma F, Shimamoto A, Tanaka K. Development of a differential optical-fiber displacement sensor. Appl Opt. 1999;38(7):1103-9. https://doi.org/10.1364/AO.38.001103.

[7] Brandão Faria JA. Modeling the Y-branched optical fiber bundle displacement sensor using a quasi-Gaussian beam approach. Microw Opt Technol Lett. 2000;25(2):138-41. https://doi.org/10.1002/(SICI)1098-2760(20000420)25:2⟨138::AID-MOP16⟩3.0.CO;2-F.

[8] Cao H, Chen Y, Zhou Z, Zhang G. Theoretical and experimental study on the optical fiber bundle displacement sensors. Sens Actuators A Phys. 2007;136(2):580-7. https://doi.org/10.1016/j.sna.2006.12.010.

[9] Huang H, Tata U. Simulation, implementation, and analysis of an optical fiber bundle distance sensor with single mode illumination. Appl Opt. 2008;47(9):1302-9. https://doi.org/10.1364/AO.47.001302.

[10] Lim KS, Harun SW, Yang HZ, Dimyati K, Ahmad H. Analytical and experimental studies on asymmetric bundle fiber displacement sensors. J Mod Opt.

2009;56(17):1838-42. https://doi.org/10.1080/09500340903366009.

[11] Yang HZ, Lim KS, Harun SW, Dimyati K, Ahmad H. Enhanced bundle fiber displacement sensor based on concave mirror. Sens Actuators A Phys. 2010;162(1):8-12. https://doi.org/10.1016/j.sna.2010.05.029.

[12] Yasin M, Rahman HA, Bidin N, Harun SW, Ahmad H. Fiber optic displacement sensor using fiber coupler probe and real objects. Sens Rev. 2012;32(3):212-6. https://doi.org/10.1108/02602281211233197.

[13] Lee CL, Shih WC, Hsu JM, Horng JS. Asymmetrical dual tapered fiber Mach–Zehnder interferometer for fiber-optic directional tilt sensor. Opt Express. 2014;22(20):24646-54. https://doi.org/10.1364/OE.22.024646.

[14] Zhang CR, Fei L, Chow PK. High-sensitivity FBG-based tilt sensor with an equal-strength beam for large structures. Opt Fiber Technol. 2019;53:102035. https://doi.org/10.1016/j.yofte.2019.102035.

[15] Guo YX, Song B, Zhao L. A wide-range FBG tilt sensor with cam-shaped transducer and improved mechanical design. IEEE Sens J. 2020;20:4740-8. https://doi.org/10.1109/JSEN.2020.2967088.

[16] Pan J, Hou W, Lin C, Bao C, Li Y. High-resolution and high-accuracy fiber-optic tilt sensor and its calibration. IEEE Sens J. 2024;24:23870-7. https://doi.org/10.1109/JSEN.2024.3409825.

[17] Sharbirin AS, Zulkifli MD, Ahmad H, Harun SW, Al-Mansoori MH. High-performance and 3D-printed two-mode fiber optic tilt sensor. J Lightwave Technol. 2019;37:1140-6. https://doi.org/10.1109/JLT.2018.2889506.

[18] Wang J, Zheng T, Huang H, Jia W, Zhou C. A bio-inspired fiber-optic attitude sensor for multi-axis tilt measurement. J Lightwave Technol. 2023;41:6844-51. https://doi.org/10.1109/JLT.2023.3294956.

[19] Guo C, Zhao Y, Zhang Z, Zhou T. A fiber-optic inclinometer based on a tapered tilted fiber Bragg grating. Opt Fiber Technol. 2015;24:30-3. https://doi.org/10.1016/j.yofte.2015.04.004.

[20] Zhao Y, Zhang Y, Feng X. An all-PCF-based reflective tilt sensor for high-sensitivity measurement. Sens Actuators A Phys. 2016;250:45-50. https://doi.org/10.1016/j.sna.2016.09.001.

[21] Li C, Zhong F, Xie H, Yan G. A wide-range tilt sensor based on a miniature liquid marble pendulum and a fiber FP cavity. IEEE Sens J. 2018;18:170-7. https://doi.org/10.1109/JSEN.2017.2777417.

[22] Zheng D, Cai Z, Floris I, Madrigal J, Pan W, Zou X, et al. Temperature-insensitive optical tilt sensor based on a single eccentric-core fiber Bragg grating. Opt Lett. 2019;44(22):5570-3. https://doi.org/10.1364/OL.44.005570.

[23] Wu C. Fiber optic angular displacement sensor. Rev Sci Instrum. 1995;66(6):3672-5. https://doi.org/10.1063/1.1145486.

[24] Wang H. Reflective fibre optical displacement sensors for the inspection of tilted objects. Opt Quantum Electron. 1996;28:1655-68. https://doi.org/10.1007/BF00331055.

[25] Yuan L, Lin X, Liang Y, Jiang Y. Applications of angled-mirror in fiber-optic sensors. Opt Laser Technol. 2000;32:255-60. https://doi.org/10.1016/S0030-3992(00)00054-2.

[26] Pal S, Verma S, Kak SK. Fiber optic sensor for angular displacement and surface slope measurement. Proc SPIE. 2001;4417:538-45. https://doi.org/10.1117/12.441349.

[27] Buchade PB, Shaligram AD. Simulation and experimental studies of inclined two fiber displacement sensor. Sens Actuators A Phys. 2006;128:312-6. https://doi.org/10.1016/j.sna.2006.02.002.

[28] Ishikawa I, Sawada R, Higurashi E, Sanada S, Chino D. Integrated micro-displacement sensor that measures tilting angle and linear movement of an external mirror. Sens Actuators A Phys. 2007;138:269-75. https://doi.org/10.1016/j.sna.2007.03.027.

[29] Khiat A, Lamarque F, Prelle C, Bencheikh N, Dupont E. High-resolution fibre-optic sensor for angular displacement measurements. Meas Sci Technol. 2010;21(2):025306. https://doi.org/10.1088/0957-0233/21/2/025306.

[30] Sakamoto JMS, Kitano C, Pacheco GM, Tittmann BR. High sensitivity fiber optic angular displacement sensor and its application for detection of ultrasound. Appl Opt. 2012;51:4841-51. https://doi.org/10.1364/AO.51.004841.

[31] Sakamoto JMS, Pacheco GM, Kitano C, Tittmann BR. Geometrical parameter analysis of a high-sensitivity fiber optic angular displacement sensor. Appl Opt. 2014;53:8436-42. https://doi.org/10.1364/AO.53.008436.

[32] Shan M, Min R, Zhong Z, Wang Y, Zhang Y. Differential reflective fiber-optic angular displacement sensor. Opt Laser Technol. 2015;68:124-8. https://doi.org/10.1016/j.optlastec.2014.10.016.

[33] Jia B, He L, Yan G, Feng Y. A differential reflective intensity optical fiber angular displacement sensor. Sensors (Basel). 2016;16(9):1508. https://doi.org/10.3390/s16091508.

[34] Zha S, Huang X, Zha C, Zhan S. Theoretical and experimental study on intensity modulation differential optical fiber angular displacement sensor. Microw Opt Technol Lett. 2021;63:1642-6. https://doi.org/10.1002/mop.32814.

[35] Zhu R, Jing R, Cheng Y. Simulation and experimental studies of a double-fiber angular displacement sensor. Opt Laser Technol. 2017;89:168-72. https://doi.org/10.1016/j.optlastec.2016.10.007.

[36] Shimizu Y, Matsukuma H, Gao W. Optical sensors for multi-axis angle and displacement measurement using grating reflectors. Sensors (Basel). 2019;19(23):5289. https://doi.org/10.3390/s19235289.

[37] Zubia G, Zubia J, Amorebieta J, Aldabaldetreku G, Durana G. A new method to design trifurcated optical fiber displacement sensors. IEEE Sens J. 2024;24(2):1532-45. https://doi.org/10.1109/JSEN.2023.3337311.

[38] Zubia G, Zubia J, Amorebieta J, Aldabaldetreku G, Zubia A, Durana G. High-performance optical fiber displacement sensor with extended linear range and sensitivity. Sensors (Basel). 2025;25(2):418. https://doi.org/10.3390/s25020418.

[39] Zubia G, Zubia J, Amorebieta J, Aldabaldetreku G, Durana G. Exhaustive analysis and simple model of an angular displacement optical fiber sensor. Sci Rep. 2025;15:19410. https://doi.org/10.1038/s41598-025-05063-4.

[40] Zubia G. Advanced optical fiber sensors for linear and angular displacement [doctoral thesis]. Bilbao: University of the Basque Country; 2025. https://doi.org/10.5281/zenodo.14917664.